City, University of London Institutional Repository

Numerical and Experimental Investigations of the Supersonic Micro Ramp Wake

Zhengzhong Sun[1], Fulvio Scarano[2], Bas W. van Oudheusden[3], Ferry F. J. Schrijer[4]

Delft University of Technology,, Delft, 2629HT, the Netherlands

and

Xiao Wang[5], Yonghua Yan[6], Chaoqun Liu[7]

University of Texas at Arlington, Arlington, TX, 76019. USA

The flow past a micro ramp immersed in a supersonic turbulent boundary layer is studied by means of numerical simulations with implicit large eddy simulation (ILES) technique and experiments conducted with tomographic particle image velocimetry (Tomo-PIV). The experimental data is mostly used to verify the validity of the numerical results by ample comparisons on the time-averaged velocity, turbulent statistics and vortex intensity. Although some discrepancies are observed on the intensity of the upwash motion generated by the streamwise vortex pair, the rates of the recovery of momentum deficit and the decay of streamwise vortex pair intensity are found in good agreement. The instantaneous flow organization is inspected making use of the flow realizations available from ILES. The flow behind the micro ramp exhibits significant large-scale unsteady fluctuations. Notably, the quasi-conical shear layer enclosing the wake is strongly undulated under the action of Kelvin-Helmholtz (K-H) vortices. The resulted vortices induce localized high-speed arches in the outer region and a deceleration within the wake associated to ejection of low-momentum fluid. Due to the presence of K-H vortex, the streamwise vortex filaments exhibit downward and outward

---

[1] Ph.D. Candidate, Faculty of Aerospace Engineering, Kluyverweg 2, 2629HT, Delft, the Netherlands, AIAA student member.
[2] Professor, Faculty of Aerospace Engineering, Kluyverweg 2, 2629HT, Delft, the Netherlands.
[3] Associate Professor, Faculty of Aerospace Engineering, Kluyverweg 2, 2629HT, Delft, the Netherlands.
[4] Assistant Professor, Faculty of Aerospace Engineering, Kluyverweg 2, 2629HT, Delft, the Netherlands.
[5] PhD Candidate, Math Deparment, 511 S. Nedderman Dr., 76019, Arlington, TX, AIAA student member.
[6] Postdoctoral Researcher, Math Deparment, 511 S. Nedderman Dr., 76019, Arlington, TX, AIAA student member.
[7] Professor, Math Deparment, 511 S. Nedderman Dr., 76019, Arlington, TX, AIAA associate fellow.

motions. The further evolution of vortical structures within the wake features the development of K-H vortices from arch shape to full ring in the far wake, under the effects of the streamwise vortices that induce an inward motion of the vortex legs and eventually connect the vortex at the bottom.

Nomenclature

A	=	area for circulation integration
c	=	micro ramp chord length, *mm*
dt	=	time interval for the stored data in ILES, laser pulse separation in PIV, *s*
H= δ^*/θ	=	incompressible boundary layer shape factor
h	=	micro ramp height, *mm*
n	=	the number of grid nodes
L	=	length of measurement volume in Tomo-PIV, *mm*
Ma	=	Mach number
Re_θ	=	Reynolds number based on boundary layer momentum thickness
U_∞	=	free stream velocity, $m \cdot s^{-1}$
U	=	time-averaged streamwise velocity component, $m \cdot s^{-1}$
V	=	time-averaged wall-normal velocity component, $m \cdot s^{-1}$
$\overline{U} = U/U_\infty$	=	normalized time-averaged streamwise velocity component
$\overline{V} = V/V_\infty$	=	normalized time-averaged wall-normal velocity component
u	=	instantaneous streamwise velocity component, $m \cdot s^{-1}$
v	=	instantaneous wall-normal velocity component, $m \cdot s^{-1}$
$\langle u' \rangle$	=	RMS streamwise velocity fluctuation, $m \cdot s^{-1}$
$\langle v' \rangle$	=	RMS wall-normal velocity fluctuation, $m \cdot s^{-1}$
$\overline{\langle u' \rangle} = \langle u' \rangle/U_\infty$	=	normalized RMS streamwise velocity fluctuation
$\overline{\langle v' \rangle} = \langle v' \rangle/U_\infty$	=	normalized RMS wall-normal velocity fluctuation
$-\overline{u'v'}, \ -\overline{u'w'}$	=	Reynolds shear stress, $m^2 \cdot s^{-2}$
$\widetilde{u'v'} = \overline{u'v'}/U_\infty^2$	=	normalized Reynolds shear stress
w	=	micro ramp width, *mm*

2

x	=	coordinate in streamwise direction, *mm*
y	=	coordinate in wall-normal direction, *mm*
z	=	coordinate in spanwise direction, *mm*

Greeks

α	=	micro ramp half span angle, degree
β	=	micro ramp trailing edge decline angle, degree
ω	=	vorticity, s^{-1}
$\overline{\omega} = \omega h / U_\infty$	=	normalized vorticity
δ	=	boundary layer thickness based on 99% of free stream velocity, *mm*
δ^*	=	boundary layer displacement thickness, *mm*
θ	=	boundary layer momentum thickness, *mm*
λ	=	wave-length, *mm*
Γ	=	circulation, $m^2 \cdot s^{-1}$

Subscript

min	=	minimum value
max	=	maximum value
KH	=	Kelvin_Helmholtz vortex
x	=	streamwise component
y	=	wall-normal component
z	=	spanwise component
$+$	=	quantity with positive value
$-$	=	quantity with negative value

I. Introduction

The micro vortex generator (MVG) is a device intended for the manipulation of boundary layer. It is a passive control technique and differs from active-control vortex generators such as boundary layer suction system and micro jet in that it does not require power input and may be of relatively simple installation. The basic principle of the MVG is that of generating a rather stable pair of counter-rotating vortices sustaining the transfer of

3

momentum from the outer region towards the wall. The MVG has been gradually recognized as an efficient tool in boundary layer flow control due to its ability to avoid or postpone flow separation. It is reported that when applied to wing-flap system in high-lift configuration, flow separation could be alleviated on the flap with consequent increase of aerodynamic performance [1]. In the turbulent boundary layer, the interaction of MVG with the wall turbulence is of complex nature. Therefore, several fundamental studies were devoted to the understanding of the flow behaviour behind MVG (Lin [2] and Yao et al. [3]). The researches on MVG in the subsonic regime has been summarized in a review paper by Lin [4].

In the supersonic regime, the use of MVG is largely associated to the control of shock wave/boundary layer interactions (SWBLI), a phenomenon occurring in supersonic inlets among other devices. Several investigations have been conducted by means of experiments and numerical simulations. In the pioneering work of Holden and Babinsky [5], the effect of micro ramps and micro vanes installed upstream of a normal shock wave was investigated and a reduction of flow separation was observed. Also, the mechanism of the streamwise pair of vortices, initially visualized in subsonic flows [2,3], was also revealed in the supersonic regime. A detailed flow topology was inferred by Babinsky et al. [6] who conjectured the existence of additional secondary vortices using oil flow visualization. A further study of Nolan & Babinsky [7] quantified the velocity field in the MVG wake by means of laser Doppler anemometry (LDA). The spatial velocity distribution in the micro ramp wake was also accessed with particle image velocimetry (PIV) within planes parallel to the flow floor by Blinde et al. [8]. Inside the velocity cross-sections, wall-normal counter-rotating vortex pairs were visualized at the edge of the micro ramp wake and were interpreted as imprints of hairpin-like vortices. A conceptual hairpin vortex model was then proposed representing the vortical structure resulting from a micro ramp.

Further understanding of the micro ramp flow organization was accomplished through numerical methods. By using implicit large eddy simulation (ILES), Li&Liu [9] visualized the ring-shaped vortices shedding from the micro ramp. Different from the streamwise vortices, the so-called "vortex rings" are active across the wake shear layer. The formation of these vortices is justified as the result of the Kelvin-Helmholtz (K-H) instability acting on the wake boundary [10-12]. Such flow instability was afterwards also confirmed by the experiments of Lu et al. [13-14] where intermittent vortical structures were evidently rolled up in the flow visualization. Sun et al. [15] have recently introduced the use of three-dimensional PIV for the study of the flow past an MVG. The measurements were performed by means of tomographic PIV (Tomo-PIV) [16,17]. By these experiments, both streamwise vortices as well as K-H vortices were measured and visualized through their vorticity. Conditional averaging technique based on K-H vortex detection also showed the initial stages of interaction between these

4

two vortex systems whereby the legs of arch-shaped K-H vortices are tilted and aligned streamwise.

According to the above investigations, there is controversy regarding the shape of the K-H vortex, and the differences of existing models concentrate on the lower part, as the leg parts of arch or hairpin vortex either maintain vertical in the cross flow plane or become parallel with the wall, whereas the filaments connect at the bottom side in the ring model. Furthermore, although the Tomo-PIV technique is able to visualize three-dimensional flow organizations, it has limited capability to extend the measurement domain following the expansion of primary wake structures, due to physical limitations of available laser pulse energy. Therefore, further investigation of the later stage of the MVG wake can be more effectively performed by means of numerical simulations. Prior to the extensive use of them, it is of paramount importance that the simulation capabilities are verified through a careful comparison with experiments.

The objective of the present study is to perform a thorough comparison between the numerical simulations obtained with the ILES technique and the experiments where Tomo-PIV is used as the diagnostic tool. The comparison is based on the velocity and vorticity statistics relevant for the MVG wake and later attention is placed on the unsteady flow organization. Furthermore, a phenomenological analysis based on the ILES results is given to solve the controversy in the existing vortex models.

II. Numerical and Experimental Cases

A. Micro ramp geometry and inflow conditions

The geometries of the micro ramps considered in the current investigation follow the work of Anderson *et al.* [18], and they are shown together in figure 1. The height of the micro ramp is h=4 mm, the chord length and half span angle are chosen at c=6.85h and α=24°, respectively. Minor modification is applied to the micro ramp device in ILES: a β=70° declining angle is added at the trailing edge, and the chord length was slightly shortened to be c=6.73h. This modification is made with the purpose of improving grid orthogonality at the trailing edge of the MVG. It has been revealed that the flow separation at the trailing region of the ramp is unaffected by this modification. Moreover, the very small value of the velocity in the small separated region in the vicinity of micro ramp has a negligible importance to the dominant features of the MVG wake.
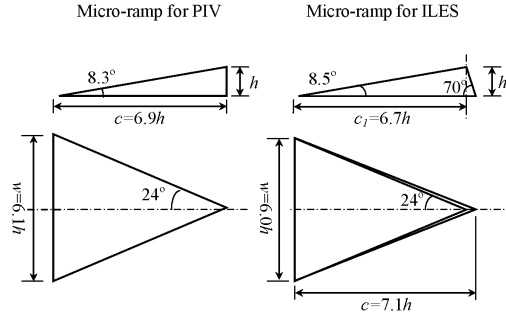
5

Fig. 1　The geometric dimensions of micro ramps for PIV (left) and ILES (right).

As the simulation was performed by solving governing equations in non-dimensional form, the relevant size parameter is given by the ratio between the device height and the undisturbed boundary layer thickness (h/δ). The undisturbed boundary layer in the wind tunnel has a thickness of 5.2 mm, h/δ is then 0.8, while this ratio is kept the same as in ILES. The Mach number in both the PIV measurements and in ILES is at Ma = 2.0. The achievable Reynolds number based on the boundary layer momentum thickness *is* Re_θ = 5760, approximately 1/3 of that in the experiment. In view of this limitations, the primary interest of present comparison is placed on the behaviour of large scale turbulent structures. The most relevant flow parameters are summarized in table 1.

Table 1　Flow parameters in ILES and PIV

Parameter	ILES	Tomo-PIV
Ma	2.0	2.0
h/δ	0.8	0.8
H	1.4	1.2
Re_θ	5760	15,740

B. The ILES simulation

Flow domain and grid generation

The dimensions of the flow domain is based on the height h of micro ramp. The length of the domain is 50h. The micro ramp is installed along the centre line of the simulation domain and 11.1h downstream of the inlet, allowing the turbulent boundary layer to reach the desired thickness. The width of the domain is 7.5h,

6

resulting an array of micro ramps layout with a distance of 7.5h between the centrelines of neighbour devices. As the conical wake is estimated to obtain a cross-flow width of approximately 4h when fully developed, it can be considered to receive trivial influence from the periodic boundary conditions applied to the sides. The height of the domain is kept constant of 10h. The origin of coordinate system is placed at the point where the micro ramp apex projected onto the floor so as to conform with the established usage of coordinate system in the literature. The detailed dimension of the computational domain is depicted in figure 2.
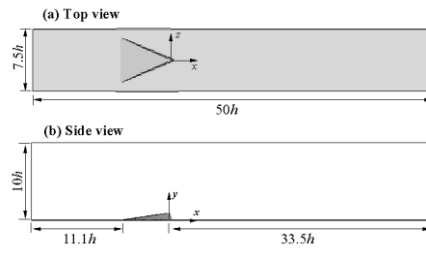

Fig. 2   Geometric dimensions of computation domain for ILES.

The simulation domain totals a number of $n_x \times n_y \times n_z$=1600×192×137 grid nodes. The entire flow domain is divided into three major grid regions, namely the initial region, the rear region and the ramp region. Wall grid clustering is applied for all the regions and y^+ for the first grid off the bottom wall is later determined to be 1.36. Uniform grids distribute in streamwise and spanwise directions in both initial and rear regions. Due to the complex geometry of the micro ramp, body fitted grids are generated to guarantee the orthogonality to a good extent. Example of the grid in the micro ramp region is shown in figure 3. In order to maintain the smooth transition from uniform grids in the initial and rear regions to the nonuniform ones in the neighbourhood of the micro ramp, two transition regions are arranged prior to and after the ramp regions. The detailed procedures for grid generation on the micro ramp region was reported in ref.[19].
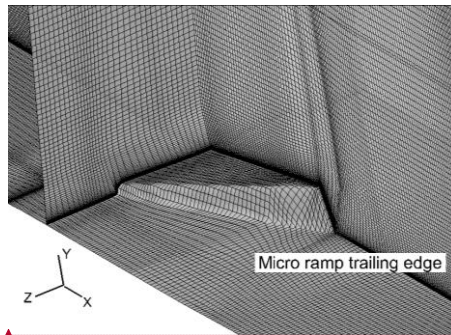

Fig. 3   Grids around the micro ramp.

7

Numerical methods

The techniques used for the present simulation, including the numerical algorithm, the treatment of boundary conditions have been carefully documented in previous works[10-12] and is only described briefly here. The Navier-Stokes (N-S) equations are solved in non-dimensional form. The ramp height represents the unit length and the fluid-dynamic properties are made non-dimensional with the free-stream flow conditions. Fifth-order WENO scheme was used for convective term discretization, while central difference is used for the viscous terms. The explicit third-order TVD-type Runge-Kutta scheme was chosen for temporal discretization. Non-slip condition was applied at the wall, periodic boundary was used for the symmetric side-walls, and non-reflection condition for the upper boundary. The inflow condition was obtained from a DNS simulation of a turbulent boundary layer[20] so that a turbulent inflow is ascertained. Analysis of the accuracy of the present code has been provided in ref. [9-11].

Spatial independence and time integration

Considering the expense of current numerical simulation, the grid resolution study was performed by increasing grid points of the baseline grid by 20% for each of the computational coordinate directions. The dense grid is thus about 1.7 times of the current one. The time-averaged velocity profiles compared between the solutions from the two grids are shown in figure 4 and the results are quite similar.

It is well known that obtaining statistically converged datasets from DNS and LES simulations is a challenge from the viewpoint of computation time and data storage. In the present work the simulation is performed for 152500 time steps after the transient shock wave pass the flow domain, corresponding to a total time of $0.62ms$. The mean flow field is achieved by averaging 305 correlated realizations. In the current simulation the physical time-marching step is estimated to be $4\times10^{-9}s$. Each 500 time-marching step ($dt=2\times10^{-6}s$) is stored in the ensemble for statistical evaluation. A convergence study of time integration for time averaging is performed by comparing velocity averaged from first 100,000 time steps and from the total 152,500 steps. A maximum error of less than 1% exists in the turbulent boundary layer prior to micro ramp device.

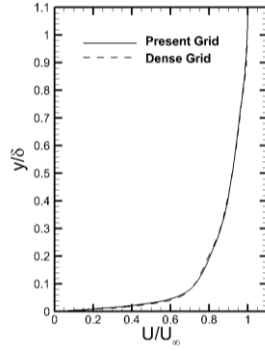Commented [LA4]: [Q] Spatial and temporal convergence

8

Fig. 4 The boundary layer profiles from different grid resolutions.

C. The Tomo-PIV experiment

The experimental results are from the Tomo-PIV measurements[15], where the detailed three-dimensional flow field structure is measured in the near wake ($9<x/h<16$). The measurements were taken in the supersonic wind tunnel ST-15 at the Faculty of Aerospace Engineering of the Delft University of Technology. The experiments contain two measurement volumes with identical size of $L_x \times L_y \times L_z=6.25h \times 4h \times 2h$, of which one was aligned with its centreline overlapping with that of the micro ramp, while the other was offset towards one side of the symmetric plane. Both measurement domains started from $x=8.75h$, their alignment is depicted in figure 5.
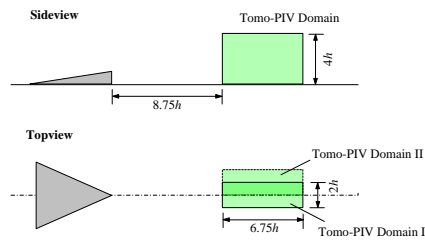
Fig. 5 Alignment of measurement domains and their dimensions in the Tomo-PIV experiment (flow direction is from left to right).

The supersonic wind tunnel was operated at Ma=2.0, the flow was seeded with di-ethyl-hexyl-sebacate (DEHS) with a nominal diameter of about 1 μm. According to the experiments performed by Ragni et al.[21], the DEHS particle tracers have a relaxation time of about 1.92 μs in a Mach 2.0 flow. Laser illumination was provided by a spectra-physics quanta ray double-pulsed Nd:Yag laser with 400 mJ pulse energy at a wavelength

9

of 532 *nm*. The particle images were recorded by three PCO Sensicam QE cameras with a CCD chip of 1376×

1040 pixels. The image acquisition was operated at 5 *Hz* through LaVision DaVis 7.2 software. Each

measurement recorded 400 image pairs to allow statistical analysis of the turbulent flow properties. Each camera

was equipped with a Nikon 105 mm focal length objective. Camera-lens tilt adapters were attached to guarantee

the Scheimpflug criterion between the image plane and the illuminated median plane. The two cameras in

forward scattering were at $f_\#$ = 16, and the camera normal to the measurement volume was at $f_\#$ = 11. The final

digital particle image resolution was 43.7 pixels/*mm*. Some further details of the experimental specifications are

listed in table 2.

Table 2 Tomographic PIV measurement parameters

Parameter	Quantity
Measurement volume	25×15×6 *mm*^{3}
Interrogation volume	1.46×1.46×1.46 *mm*^{3}
Digital image resolution	43.7 pixel/*mm*
Object focal length	*f*=105 *mm*
$f_\#$	$f_\#$ = 11, 16
Laser pulse separation	0.6 μs
Seeding density	0.05 particle/pixel

The detailed procedures of uncertainty determination is reported in ref.[15], thus only the key parameters are cited here in table 3. The uncertainty of time-averaged quantities is affected by the limited ensemble size, which contains 400 uncorrelated velocity fields. The uncertainty of time averaged velocity is estimated to be 0.8% U_∞ inside the wake region. The uncertainties of the RMS of *u* and Reynolds shear stress are determined to be 5%<*u'*>$_{max}$ and 50%$\overline{u'v'}$ $_{max}$, respectively. The uncertainty of instantaneous velocity is primary determined by the three-dimensional cross-correlation. A value of 0.2 voxel is conservatively assumed for the present measurement, corresponding to about 0.5% of the free stream velocity. The particle response time τ_p also affects the measurement fidelity. The particle slip is quantified by multiplying the particle slip time τ_p (for DEHS particle τ_p =1.92μs) with a relevant acceleration a_p. In the current micro ramp flow, the most relevant acceleration happens at vortex region, where centrifugal acceleration is exerted and is about 5.3×10^6 *m/s*^{2}. As a result, the velocity uncertainty due to particle slip is estimated about 2% U_∞.

Commented [LA6]: Uncertainty of Tomo-PIV measurement

Table 3. Uncertainty parameters of Tomo-PIV measurement

Parameter	Quantity
Statistical uncertainty $\varepsilon_{\bar{u}}/U_\infty$	0.8%
Cross-correlation uncertainty ε_{cc}	0.2 voxel
Instantaneous velocity $\varepsilon_{u(\varepsilon_{cc})}/U_\infty$	0.5%
Velocity fluctuation $\varepsilon_{\langle u'\rangle}/\langle u'\rangle_{max}$	5%
Reynolds shear stress $\varepsilon_{\overline{u'v'}}/\overline{u'v'}_{max}$	50% (wake region)
Particle slip $\varepsilon_{\tau p}/U_\infty$	2%

III. Results and Discussion

The time-averaged flow properties, including mean velocity (U, V), turbulent statistics ($\langle u'\rangle$, $\langle v'\rangle$, Reynolds shear stress) , vorticity and circulation associated to streamwise vortex pair, are firstly compared. The above comparison represent a crucial step for the validation of turbulence simulation capabilities. The instantaneous flow features are compared at a qualitative level by inspecting snapshots, in order to give a general characterization of the pattern of large-scale motions. Finally, attention is placed on the unsteady organization of coherent vortices that dominate the dynamics of wake flow.

A. Comparison of time-averaged flow properties

Turbulent boundary layer

The turbulent boundary layer in the immediate upstream of the micro ramp predicted in ILES and that measured by PIV are compared in figure 6. The velocity is normalized by the free stream magnitude U_∞, which will be adopted in the following analysis. The prediction of ILES results in a turbulent boundary layer with less full profile, indicating a slight larger shape factor H. The discrepancy in the two profiles becomes larger when closer to the wall, resulting in different velocity gradients. The Reynolds number effect could be one reason, while the measurement uncertainty may also take effect, as the measurement in the near wall region are affected by a higher uncertainty due to the light reflection and low particle density than in the region away from the wall.
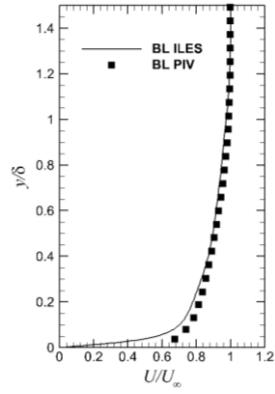
Fig. 6 Comparison of boundary layer profile in the immediate upstream of micro ramp

Mean flow field

The mean velocity contours of normalized streamwise and wall-normal velocity component at three streamwise stations (x/h = 10, 12 and 14) are presented in figure 7. The comparison of ILES and PIV results is made with the ILES on the left half and PIV on the right half. The wake exhibits a circular shape away from the wall with u-deficit and a neck region that connects it to the wall. Moving downstream from x/h=10 to 14, a wake recovery is observed, with the minimum streamwise velocity increasing from $0.6U_\infty$ to $0.7U_\infty$. The wake is also lifted away from the wall while moving downstream as expected under the induction of the streamwise vortex pair. The comparison between the ILES and PIV results indicates that, despite the similar general appearance, the wake obtained by ILES has a higher position at x/h = 10 than that measured with PIV. The difference, however, vanishes already at x/h =14. The faster rate of lifting off the surface observed in the experiments is consistent with the more intense upwash measured in the wake centre (figure 7 bottom row).

Further comparison is made by extracting the profiles of U within the centre plane, as plotted in figure 8. According to the previous study[12], the centre plane intersects the wake at two points of the shear layer. Therefore, in the profiles two shear layers are observed: the strongest one delimits the wake on the upper edge, whereas the lower one delimits the wake from the near-wall region. The shear layers in figure 8 from both ILES and PIV overlap to a good degree, although the thickness and the position of the upper shear from ILES are slightly overestimated at x/h=10. The faster recovery of wake deficit for the ILES results is especially evident at x/h=14.
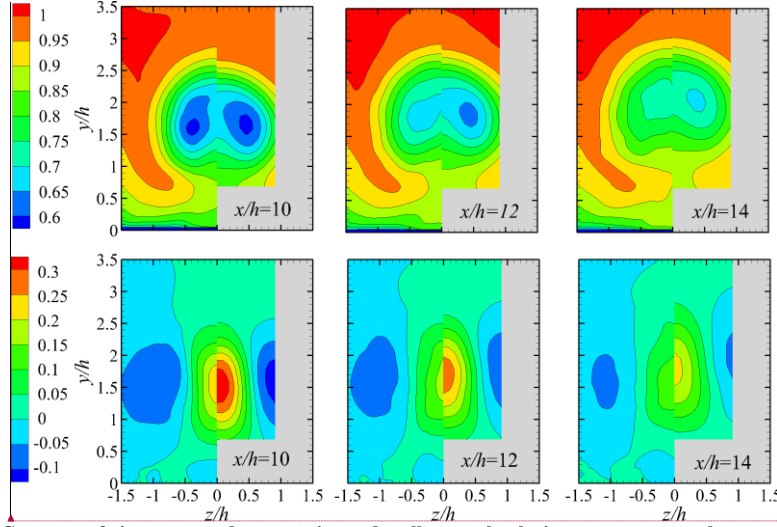
12

Fig. 7 Contours of time-averaged streamwise and wall-normal velocity component at three streamwise positions (*x/h*=10 ,12 and 14). In each plot, the left half is from ILES and the right half is from Tomo-PIV. Top row: contours of *U/U*∞, bottom row: contours of *V/U*∞.
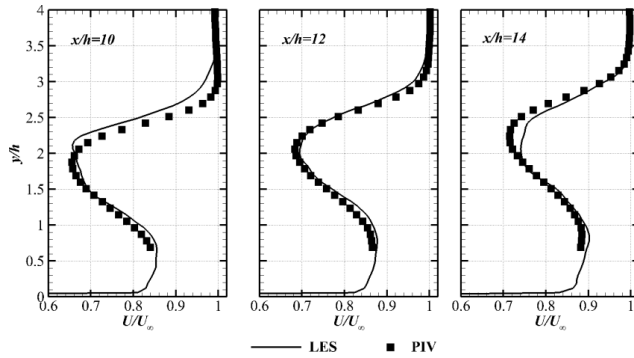

Fig. 8   Profiles of streamwise velocity component in the center plane at three positions of *x/h*=10, 12 and 14.

The distribution of wall-normal velocity component is also an important flow feature as it is directly associated to the intensity of the flow induced by the streamwise vortex pair, namely a vigorous upwash motion at the center and a more diluted downwash on the sides. By comparing the contours in the lower row of figure 7, the strength of both upwash and downwash motions obtained by the ILES appears to be less than that measured with PIV. The detailed comparison is provided by the *V*-profiles at the center plane as plotted in figure 9. The peak upwash is measured to be V_{max}=0.34U_∞ by PIV at x/h=10, while a reduced peak of 0.24U_∞ is estimated by

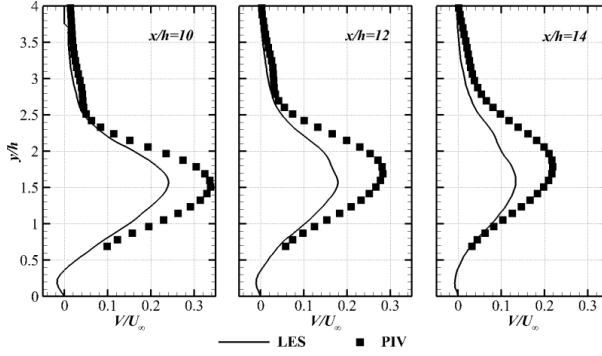ILES. This difference was maintained till the downstream stations.

Fig. 9   Profiles of wall-normal velocity component in the center plane at three positions of *x/h*=10, 12 and 14.

Turbulent statistics

The velocity fluctuations are estimated through the root-mean-square (RMS) of each velocity component. The distributions of $\langle u' \rangle$ and $\langle v' \rangle$ within a cross-flow plane at *x/h*=12 are plotted in figure 10, with the left half being ILES result and the right half PIV result. According to figure 10(a), peak fluctuations of streamwise velocity can be observed along the averaged quasi-circular shear layer, where the flow instability produces streamwise acceleration and deceleration of significant amplitudes. The spatial distribution of the streamwise velocity fluctuation returns a marked discrepancy between ILES and PIV results. It can be seen that $\langle u' \rangle_{max}$ is slightly overestimated by ILES and it follows the shear layer better than the results of PIV, which does not show a peak at the top region, where it would be expected. The peak fluctuation of wall-normal velocity $\langle v' \rangle_{max}$ concentrates in the inner wake. These fluctuations are also regarded as a result of the flow shear layer instability, which undulates the flow in vertical direction at the upper edge of the wake.
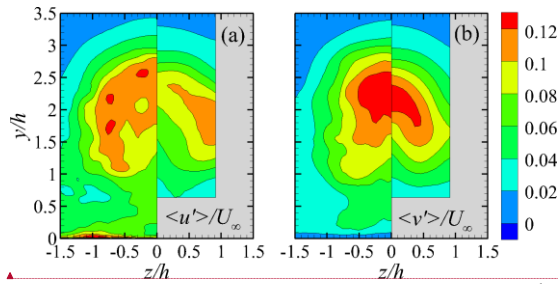

Fig. 10   Contours of velocity fluctuations at *x/h*=12: (a) streamwise component $\langle u' \rangle$, (b) wall-normal component $\langle v' \rangle$.

The Reynolds shear stress components from the same cross-flow plane at x/h=12 are compared in figure 11.

As $-\overline{u'v'}$ is a measure of the shear stress in the vertical direction, positive peaks are expected in the top part of the shear layer, where vertical mixing is the major activity. Accordingly, symmetric peaks of $-\overline{u'w'}$ are produced on both sides of the shear layer. Both ILES and PIV reveal a consistent distribution of Reynolds shear stress, although the magnitude is higher in the ILES results. In order to reveal the two components of Reynolds shear stress as a whole, squared root of the two components is computed and plotted in figure 11(c).

The region containing peak values clearly follows the curvature of shear layer, notifying the shear activity involved. This observation is further clarified by the presence of three dimensional large-scale structures produced by the instability of the quasi-circular shear layer.
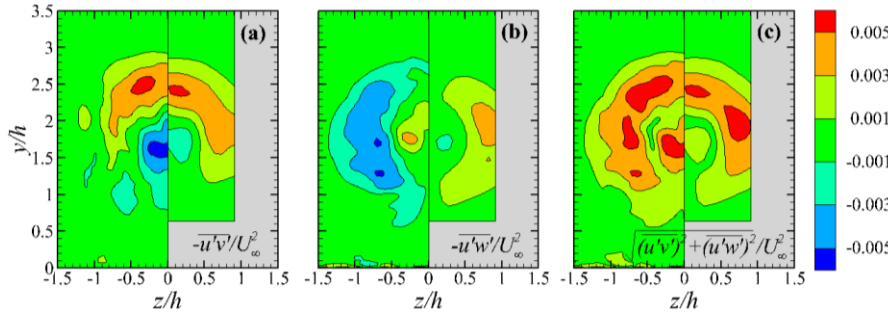

Fig. 11   Contours of Reynolds shear stress components at x/h=12: (a) $-\overline{u'v'}$**, (b)** $-\overline{u'w'}$**, (c)**

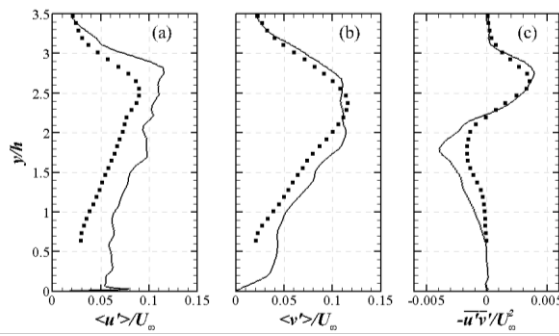$$\sqrt{\overline{u'v'}^{2}+\overline{u'w'}^{2}}$$

Fig. 12   Profiles of turbulence quantities in the centre plane at x/h=12: (a) $\langle u'\rangle$**, (b)** $\langle v'\rangle$**, (c)**

$$-\overline{u'v'}.$$

15

A detailed evaluation is made through comparison of wall-normal profiles at the centre plane of the wake. The profiles of $\langle u'\rangle$, $\langle v'\rangle$ and $-\overline{u'v'}$ at x/h=12 are plotted in figure 12. The largest discrepancy is found for the streamwise velocity fluctuations $\langle u'\rangle$, which is predicted about 25% larger by ILES than the PIV results. Nevertheless, the spatial distribution is very similar with a sharp increase moving from outside the wake through the upper shear layer. The comparison of $\langle v'\rangle$ profiles in figure 12(b) returns a good agreement, although the ILES result features a plateau region at the maximum rather than a concentrated peak. The Reynolds shear stress $-\overline{u'v'}$ comparison also agrees rather well for the upper shear layer, whereas a larger discrepancy is observed in the lower portion of the wake. In recent planar PIV measurements dedicated to the decay of the micro ramp wake [22], symmetric peaks of $-\overline{u'v'}$ were observed with positive peak at the upper shear layer and negative peak at the wake centre. Hence the ILES approximation can be considered reasonable.

Time-averaged streamwise vortices

It has been revealed that the primary streamwise vortex pair is the major working mechanism of the micro ramp device[6], and an accurate prediction of the vortex strength is crucial for further investigation of the control effect towards SWBLI. The streamwise vortex filaments are thus paid special attention and compared in terms of peak streamwise vorticity component and circulation magnitude, as these two terms represent the vortex strength and have been studied in the other studies [3,23].
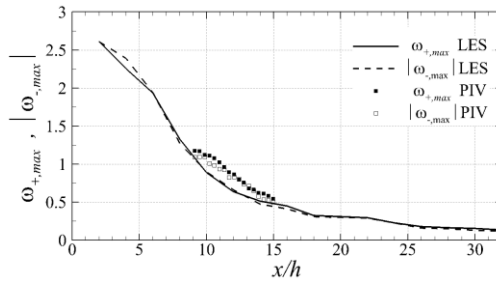

Fig. 13   Comparison of the streamwise evolutions of peak streamwise vorticity, normalized by U_∞/h.

The comparison of peak streamwise vorticity magnitudes is addressed in figure 13, where a rapid exponential decay of streamwise vortices is exhibited through the evolution of maximum vorticity. Till downstream at approximately x/h=18, the decay slows down and the peak vorticity reduces to about 1/10 of that

16

when it is freshly produced at x/h=2. Due to the limitation of Tomo-PIV measurement, the comparison can only be conducted within a streamwise portion of x/h=9~16. According to current comparison, the predicted decay trend follows that of measurement, but with slightly lower strength. Since the upwash is a direct product of the vortical activity, and is thus determined by vortex intensity. The weaker upwash as revealed earlier can be ascribed to underestimation of streamwise vortex strength. There are also other literatures on the peak vorticity evolution of MVG. In the ILES work of Lee et al.[23] on the Mach number effects of the micro ramp wake, similar exponential decay of streamwise maximum vorticity was revealed at three Mach numbers and at the point of x/h=30, $\omega_{x,max}$ was also about 1/10 of the strength when at immediate downstream of micro ramp. Yao et al.[3] also measured the vortex evolution produced by micro vane using Stereo-PIV in subsonic flow of U_∞ =34m/s, the maximum streamwise vorticity at x/h=30 also decreased to about 1/10 of that at the most upstream.
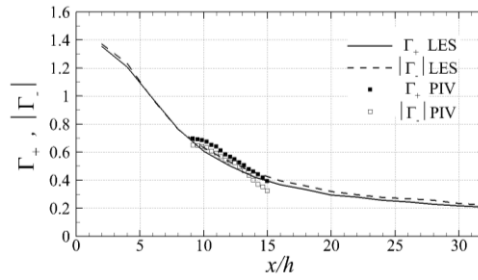

Fig. 14   **The streamwise evolution of streamwise vortex induced circulation *Γ*, normalized by $U_\infty h$.**

Vortex induced circulation is an alternative for vortex strength assessment. In the current micro ramp flow, the circulation associated with streamwise vortex is calculated through

$$\Gamma = \iint_A \omega_x \, dydz$$

where A is the integration area in cross flow plane. For current comparison study, A is chosen to be the area of cross-section in measurement II in the Tomo-PIV experiments for both simulation and measurement results. The resulted circulation of both ILES and PIV are compared in figure 14. The circulation is observed to develop in a less steep way than the maximum vorticity and Γ at x/h=30 is about 1/7 of the most upstream magnitude. In addition, the comparison of the circulation obtains a smaller discrepancy than that of maximum vorticity. In the experimental study of Yao et al.[3], the circulation evolution was evaluated as well, where a similar decay of

circulation could also be observed. However, it took more than 100 device heights to reduce to 1/7 of the most upstream strength, suggesting less dissipative property of vortex when the device is used in subsonic flows.

In conclusion, the above comparisons yield an impression of the overall ILES accuracy. The streamwise velocity, turbulent statistics and vortex related circulation are in relatively good agreement with experiments. A discrepancy on the upwash intensity is displayed and ascribed to the vortex strength underestimation.

B. The instantaneous velocity field

The flow topology of the instantaneous realization is expected to differ remarkably from that observed on the mean, as large-scale fluctuation driven by the Kelvin-Helmholtz instability takes effect. The instantaneous wake flow is represented through the streamwise velocity contours in cross-flow planes at four stations, namely x/h=1,10,20,30 (see figure 15), where the vortices can be identified through overlaid vectors. A good degree of symmetry, in terms of velocity distribution and vortex positions, is exhibited within the wake at the immediate downstream of the micro ramp, see the velocity contour at x/h=1 (figure 15(a)), suggesting that the instability effect is less dominant at this stage. The two primary vortices are produced nearly at the same height of about 0.5h above the wall. A pair of secondary vortices can be observed in the vicinity of wall due to the shearing between the primary vortex and wall. The secondary vortices are prominent flow structures in the near wake region and have been addressed by several authors. Babinksy et al.[6] revealed the secondary vortex filaments though oil flow visualization and they are later included in the model describing mean vortical structure.
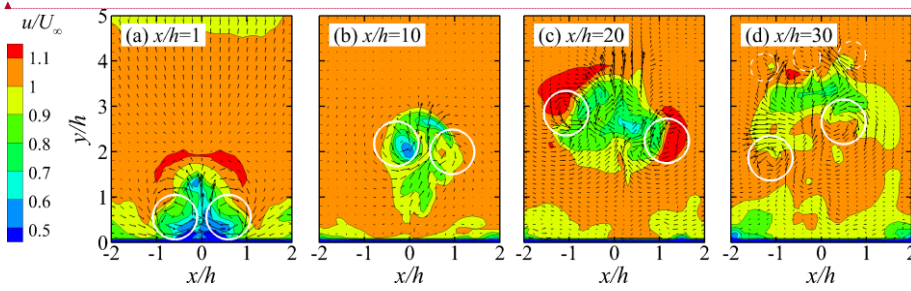

Fig. 15 Contours of instantaneous velocity in cross-flow planes at different streamwise stations, three-dimensional vectors are projected for vortex visualization.

In the flow cross section at x/h=10 (figure 15(b)), the wake containing low momentum fluid elevates to about y=2h, and becomes barely symmetric by tilting to one side, suggesting that the flow unsteadiness takes effect and undulates the wake structure. The primary streamwise vortices follow the wake elevation and obtain a

18

height of approximately 2*h* and have a lateral distance of about 1.5*h*, which is similar as in *x/h*=1. The secondary vortices close to the wall cannot be observed in the current plane, as the shear between primary vortex and wall vanishes once the vortices are lifted sufficiently high. By inspecting the lateral cross sections in the current flow snapshot, it is found that secondary vortices persist till about three ramp heights downstream. In the surface flow visualization of Lu et al.[13], the secondary vortices survived untill about 3.5*h* downstream according to the oil tracks in the visualization image. Since the primary vortices are anticipated to stay close to the wall to execute maximum boundary layer flow control, and the secondary vortices are also able to assist momentum exchange in a smaller spatial scale as well, it could be inferred that the control effect deteriorates once the wake lifts up.

The wake cross-section at *x/h*=20 grows further (figure 15(c)). The wake deficit region expands to a width of about 2*h* and is elevated to about 2.5*h*. Velocity recovery can be observed at current plane as the minimum deficit velocity increases to $0.7U_\infty$. Following the wake expansion, the distance between two streamwise vortex filaments increases to about 2*h* and they are not at the same height. The wake at *x/h*=30 (figure 15(d)) becomes significantly distorted, however, the height of wake is maintained the same as that in *x/h*=20, suggesting a horizontal wake far downstream. Due to the turbulent diffusion that takes place in the micro ramp wake, the intensity of vortices becomes rather weak, as they are of similar strength of turbulent eddies, which are indicated through dashed circles.

C. Flow instability at the wake edge

The K-H instability that happens at the wake edge is another notable structure in the micro ramp wake, since it is a three-dimensional phenomenon and has the major extension in streamwise direction, two cross-sections encompassing the center plane (*z*=0) and the horizontal plane at two ramp heights (*y/h*=2) are utilized for discussion, see figure 16. Note that the two planes are extracted from the same flow snapshot in figure 15. The flow instability at the wake edge is characterized by the wave-like boundary enclosing the micro ramp wake. Different from the time-averaged flow, the instantaneous wake region has a series of intermittent packets containing high or low speed respectively, which are produced following the local flow motion enforced by the K-H vortex. In order to provide detailed observation on the interaction between K-H vortex and the surrounding flow, the rear part of the horizontal cross section from *x/h*=24 to 30 is enlarged in figure 17. Note that a constant value of $0.87U_\infty$ has been subtracted from streamwise vector component for vortex visualization. The vortices identified by the solid circles are the cross sections of K-H vortices. According to the motion of swirling vectors, acceleration and deceleration appear on the outer and inner sides of the wake edge respectively,

19

leading to the generation of separate velocity packets eventually. Since the micro ramp wake expands wide enough and reaches about $3h$ in width at the end of the domain, secondary event is possible inside the wake region. A secondary vortex pair inside the wake with counter rotation can be observed and is indicated with dashed circles. This phenomenon was also visualized experimentally by Sun et al.[15].
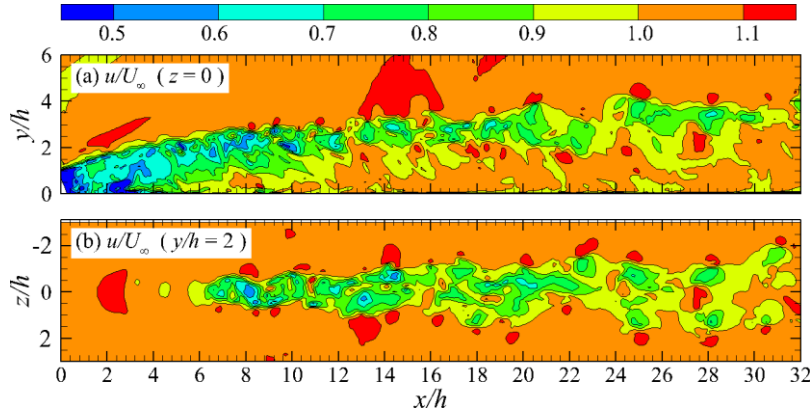

Fig. 16 Instantaneous flow cross-sections of streamwise velocity, (a) center plane at z=0, (b) horizontal plane at y/h=2.
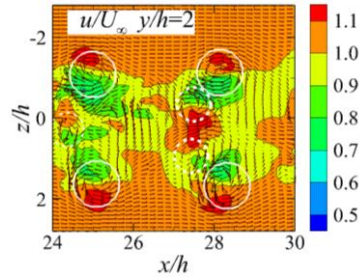

Fig. 17 An enlarged view of the horizontal plane at y/h=2 in figure 16, the vortices are visualized by subtraction of a constant value of $0.87U_\infty$ from the streamwise vector component.

Although flow instability is present on both the top and bottom edges of the far wake in figure 16(a), difference can be observed in the near wake region, where the K-H instability phenomenon on the bottom side only appears after x/h=8. As revealed by Yan et al.[12], the flow instability is associated to the inflection point in

20

the shear profile. The delayed generation in the lower side can thus be attributed to the late formation of the shear layer in the bottom side.

The growth of flow instability can also be evaluated through the increase of wave-length of the unstable wave, namely the distance between two K-H vortices. According to the vortex visualization in figure 17, the streamwise distance is about $3h$ at x/h=26 while that in the upstream at x/h=8 is only $1h$. The ample increase of the wavelength is the outcome of vortex pairing, through which two vortices merge into one and the wavelength is doubled. One pairing process taking place in the center plane of figure 16(a) is enlarged in figure 18. Note that an identical operation as in figure 17 is performed to visualize the vortices. According to the visualization, two K-H vortices at around x/h=17 obtain a closer distance of $0.5h$ and are about to merge.
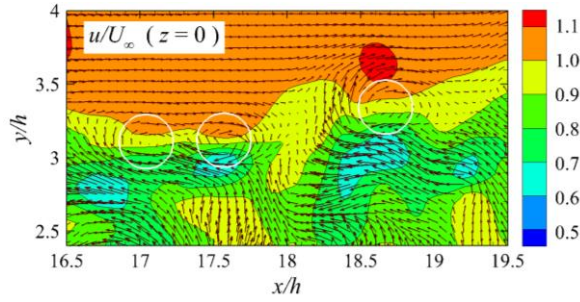

Fig. 18 An enlarged view within the symmetry plane.

D. Vortical organization

The micro ramp wake contains streamwise vortices and K-H vortices induced through the shear layer instability, a complete description of the vortical organization is thus of great importance leading to an optimized use of the device. In this section, an overview of the evolution of vortical organization is provided, after which one typical K-H vortex is studied following its temporal evolution.

The top and side views of the vortical field deduced from the same flow realization in the previous discussions are provided in figure 19. While the streamwise vortex filaments are represented through the iso-surfaces of ω_x (red and blue), the K-H vortex is represented through iso-surfaces of $\omega_{KH} = \sqrt{\omega_y^2 + \omega_z^2}$ (green) as it has the major dimension in the y-z plane.

The visualized vortical organization first of all confirms the co-existence of the streamwise vortex and K-H vortex, which has been revealed by Sun et al.[14]. The aforementioned growth of flow instability can be observed more straightforwardly through the relevant K-H vortices. The increased wavelength of the unstable

21

wave is represented through the larger streamwise distance between the adjacent three-dimensional K-H vortices.

Following the development of the micro ramp wake, large scale motions are exhibited by the vortices. While the K-H vortices are regularly aligned in the near wake ($x/h<10$), they undergo undulations in the lateral plane further downstream, where notable motions in spanwise and wall-normal directions can be observed. Similarly, motions of streamwise filaments are also exhibited in close relation with the presence of K-H vortex, whereas they are nearly parallel in the near wake. The downward and outward motions as indicated in figure 19 may eventually lead to the merge with K-H vortex.
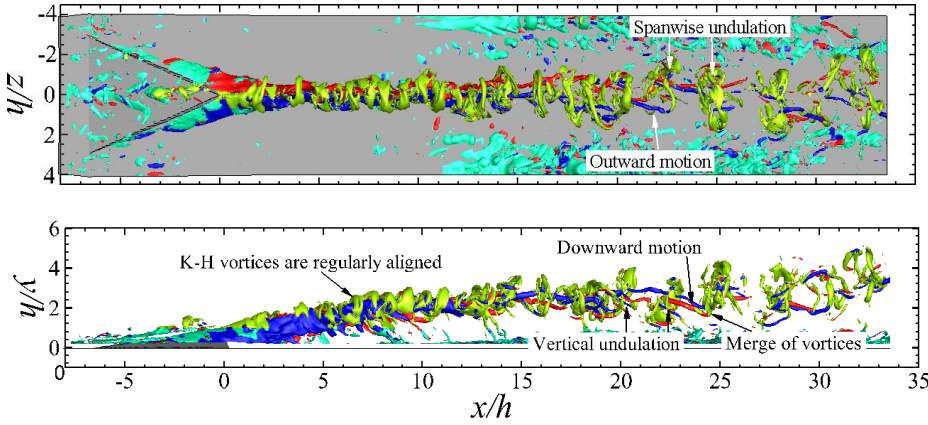
Fig. 19 The vortical field represented through vorticity iso-surfaces, light green: iso-surface of $\omega_{KH} = \sqrt{\omega_y^2 + \omega_z^2}$, red: iso-surface of $\omega_x<0$, blue: iso-surface of $\omega_x>0$. Upper: topview; Lower: sideview.

In order to clarify the controversy on the vortex shape that introduced earlier, the evolution of one K-H vortex generated at around time $t_0=66dt$ is studied. Since the chosen vortex can be tracked almost till the end of current simulation, three significant evolution stages are selected to display the corresponding characteristics, see figure 20. Following the foregoing analysis, ω_{KH} is again used for K-H vortex identification. While the high-speed packet is the product of vortical motion, it must follow the shape of K-H vortex. As a result, the iso-surface of streamwise velocity equalling $1.1U_\infty$ (red in color) is plotted in addition to the vorticity iso-surface.

The K-H vortex in the near wake of x/h=6 (figure 20(a)) is visualized through iso-surface equalling $\overline{\omega}_{KH} =$ 2.1 (light blue). It is evident that the K-H vortex at this stage is of an arch shape, which conforms to the description of Sun et al.[15]. As anticipated, the high-speed packet follows the curvature of the K-H vortex, and consequently displays similar arch shape with slightly larger diameter. Recalling the flow cross-sections in figure 16, the high speed blobs located at the exterior of the wake is actually cross-sections of the high-speed arch.

When in the intermediate stage at x/h=10, the K-H vortex is also visualized through iso-surface of $\overline{\omega}_{KH}$=2.1 (figure 20(b)), however difference is displayed, as the leg portion of the arch vortex exhibits substantial extension and finally curved into the bottom side of the wake. The inward motion of the leg portion is primary ascribed to the rotation enforced by the streamwise vortex. For the purpose of explanation, vectors in the lateral plane at x/h=9.5 are projected to visualize the vortical motion (figure 20(b)). The axis of the counter-rotating vortex pair are inclined towards left-hand side while there is one smaller vortex cross-section below. Considering the flow motion induced by the primary vortex pair, downward trend is resulted and is followed by the inward motion (see the red arrows in figure 20(b)), which eventually force the K-H vortex to penetrate into the lower side. Another reason of the vortex inward motion could be the elevation of the wake region, which allows formation of shear layer from the bottom side and eventually gives rise to K-H vortex there. The high-speed packet resembles the K-H vortex and is also shown in figure 20(b), where the extended legs are especially clear.

This K-H vortex keeps on growing, and its appearance at x/h=20 is shown in figure 20(c). The K-H vortex is visualized using iso-surface of $\overline{\omega}_{KH} = 1.6$, a smaller value than previous two, suggesting the decay of vortex intensity. In the current visualization, the curved legs of K-H vortex connect at the bottom side and a full ring is formed. Accordingly the induced high speed packet also obtains a similar ring shape at the outer edge, which is also revealed through velocity iso-surface of u=1.1U_∞ in figure 20(c). So far it can be seen that the ring vortex model of Li&Liu[8] only describes the K-H vortex in the far wake instead of the entire development. If close attention is switched to the bottom side of the ring vortex, the vortex filament stretches into the wake core and forms a concave ring. So far the K-H vortex has been detected to appear as arch-shaped and ring-shaped at different evolution stages, the former is dominant in the near wake region, while the latter is mostly formed in the far wake. The transition from arch to ring is fulfilled through inward movement of leg portion induced by streamwise vortex filaments. As a result, the existing vortex models only feature the K-H vortex in a partial stage.
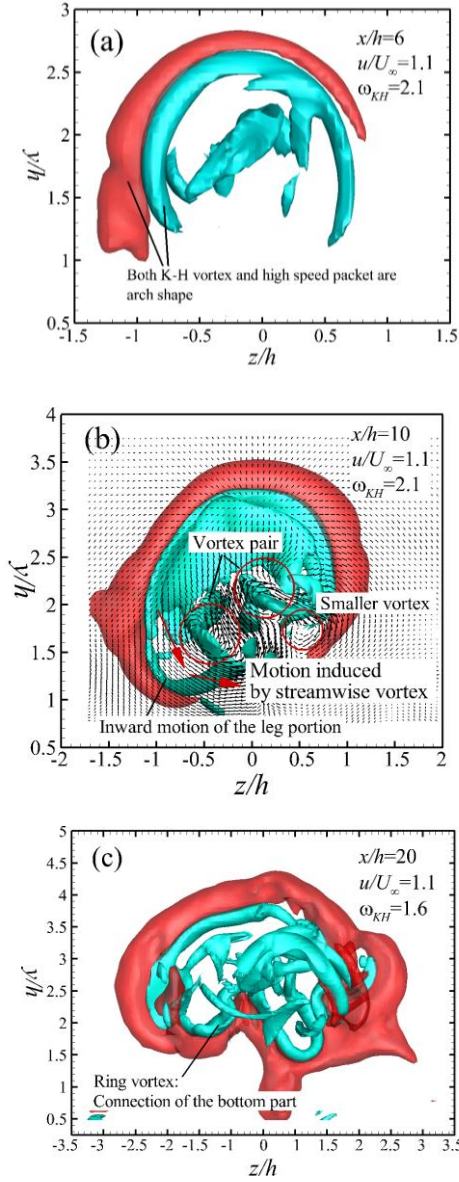
23

Figure 20. Time evolution of one K-H vortex: (a) early stage: arch-shaped K-H vortex at *x/h*=6; (b) intermediate stage: arch-shaped K-H vortex with inward curved legs at *x/h*=10; (c) fully developed stage: ring-shaped K-H vortex at *x/h*=20. High-speed packet is represent through iso-surface of streamwise velocity with *u/U∞*=1.1 (red), K-H vortex is represented through iso-surface of ω_{KH} (light blue).

IV. Conclusions

The wake produced by the micro ramp immersed in a supersonic turbulent boundary layer is investigated by means of ILES. An extensive comparison with Tomo-PIV measurement is performed on the statistical flow properties. Agreement of streamwise velocity, turbulent statistics, vortex circulation is observed, however, discrepancy exists in the wall-normal velocity component, which is reasoned as the underestimation of the strength of streamwise vorticity.

Analysis has been carried out based on the flow realizations from simulation. The wake is observed to lift off the surface with its streamwise evolution and becomes nearly horizontal in the far wake. The instantaneous wake is featured with flow instability of K-H type and the associated vortical structure, namely the K-H vortex. Instability phenomenon grows in the current realizations and is characterised by the increased wavelength of the unstable wave, which is fulfilled through vortex pairing process. The streamwise filaments was revealed to exhibit distinctive behaviours in different flow regions. While they appear as focused filaments in streamwise direction, outward and downward motions are significant in the far wake causing the merge with the leg portions of K-H vortex.

The controversy on the appearance of K-H vortex has been clarified. Since flow instability is not developed in the lower side of the wake close to the device trailing edge, it is initially generated as arch-shaped vortex. A similar arch but with inward-extended legs is present in the intermediate region. The inward motion is terminated when the ring vortex is formed. As a result, the K-H vortex develops from arch shape to ring and a progressive model is needed to describe the vortical organization in the micro ramp wake.

References

[1] Lin, J. C., Separation control on high-lift airfoils via micro-vortex generators, J. Aircraft, 31(1994).

[2] Lin, J.C., Control of turbulent boundary-layer separation using micro-vortex generators, AIAA paper 199-3404.

[3] Yao, C-S, Lin, J. C. and Allan, B. G., Flow-field measurement of device-induced embedded streamwise vortex on a flat plate, AIAA paper 2002-3162.

[4] Lin, J. C., Review of research on low-profile vortex generator to control boundary-layer separation, Progress in Aerospace Sciences, 38(2002), 389-420.

[5] Holden, H. and Babinsky, H, Effect of microvortex generators on separated normal shock/boundary layer interactions, J. Aircraft, 44(2007), 170-174.

[6] Babinsky, H., Li, Y. and Pitt Ford, C. W., Microramp control of supersonic oblique shock-wave/boundary-layer interactions, AIAA J. 47(2009), 668-675.

[7] Nolan, W. R. and Babinsky, H., Characterization of micro-vortex generators in a supersonic flows, AIAA paper 2011-71.

[8] Blinde, P. L., Humble, R. A., van Oudheusden, B. W. and Scarano, F., Effects of micro-ramps on a shock wave/turbulent boundary layer interaction, Shock Waves, 19(2009), 507-520.

[9] Li, Q. and Liu, C., LES for supersonic ramp control flow using MVG at M=2.5 and Re=1440, AIAA paper 2010-592.

[10] Yan, Y., Li, Q., Liu, C., Pierce, A., Lu, F. and Lu, P., Numerical discovery and experimental confirmation of vortex ring generation by microramp vortex generator, Appl. Math. Modell. 36(2012), 5700-5708, doi:101016/j.apm.2012.01.015.

[11] Yan, Y., Chen, C., Wang, X. and Liu, C., LES study on the mechanism of vortex rings behind supersonic MVG with turbulent inflow, AIAA paper 2012-1093.

[12] Yan, Y., Li, Q., Liu, C. and Lu, F., Numerical, experimental and theoretical studies on mechanism of K-H instability and ring generation behind supersonic MVG, AIAA paper 2011-676.

[13] Lu, F. K., Pierce, A. J. and Shih, Y., Experimental study of near wake of micro vortex generators in supersonic flow, AIAA paper 2010-4623

[14] Lu, F. K., Li, Q. and Liu, C., Microvortex generators in high-speed flow. Progress in Aerospace Sciences, 53(2012), 30-45, http://dx.doi.org/10.1016/j.paerosci.2012.03.003.

[15] Sun, Z., Schrijer, F. F. J., Scarano, F. and van Oudheusden, B. W., The three-dimensional flow organization past a micro-ramp in a supersonic boundary layer, Phys. Fluids, 24(2012), http://dx.doi.org/10.1063/1.4711372.

[16] Elsinga, G. E., Scarano, F., Wieneke, B. and van Oudheusden, B. W., Tomographic particle image velocimetry, Exp. Fluids, 41(2006) 933-947, doi:10.1007/s00348-006-0212-z.

[17] Scarano F., Tomographic PIV: principles and practice. (Review Article) Meas. Sci. Technol., 24(2013), doi:10.1088/0957-0233/24/1/012001.

[18] Anderson, B. H., Tinapple, J. and Surber, L., Optimal control of shock wave turbulent boundary layer interactions using micro-array actuation, AIAA paper 2006-3197.

[19] Li, Q. and Liu, C., Declining angle effects of the trailing edge of a microramp vortex generator, J. Aircraft, 47(2010).

[20] Liu, C. and Chen, L., Study of mechanism of ring-like vortex formation in late flow transition, AIAA paper 2010-4623.

[21] Ragni, D., Schrijer, F., van Oudheusden, B.W., Scarano, F., Particle tracer response across shocks measured by PIV, Exp. Fluids 50(2011).

[22] Sun, Z., Schrijer, F. J. J., Scarano, F. and van Oudhensden, B. W., Decay of the micro-ramp wake in the symmetric plane, 8th international symposium on turbulence and shear flow phenomena, Poitiers, France, 2013, August

[23] Lee S., Loth, E., Georgiadis, N.J. and DeBonis, J.R., Effect of Mach number on flow past microramps, AIAA J. 49(2011).